

The *Kepler* Smear Campaign I: An Asteroseismic Catalogue of Bright Red Giants

Benjamin J. S. Pope,^{1,2,3*} Guy R. Davies,^{4,5} Keith Hawkins,^{6,7} Timothy R. White,^{5,8}
Daniel Huber,^{9,10,11} Ashley Chontos,⁹ Victor Silva Aguirre,⁵ Victoria Antoci,⁵
Suzanne Aigrain,³ Timothy R. Bedding,^{10,5} Jie Yu,^{10,5} Amalie Stokholm,⁵
Timothy van Reeth,^{5,10} and friends

¹Center for Cosmology and Particle Physics, Department of Physics, New York University, 726 Broadway, New York, NY 10003, USA

²NASA Sagan Fellow

³Oxford Astrophysics, Denys Wilkinson Building, University of Oxford, OX1 3RH, Oxford, UK

⁴School of Physics and Astronomy, University of Birmingham, Birmingham B15 2TT, UK

⁵Stellar Astrophysics Centre, Department of Physics and Astronomy, Aarhus University, Ny Munkegade 120, DK-8000 Aarhus C, Denmark

⁶Department of Astronomy, The University of Texas at Austin, 2515 Speedway Boulevard, Austin, TX 78712, USA

⁷Department of Astronomy, Columbia University, 550 W 120th St, New York, NY 10027, USA

⁸Research School of Astronomy and Astrophysics, Mount Stromlo Observatory, The Australian National University, Canberra, ACT 2611, Australia

⁹Institute for Astronomy, University of Hawai'i, 2680 Woodlawn Drive, Honolulu, HI 96822, USA

¹⁰Sydney Institute for Astronomy (SIfA), School of Physics, University of Sydney, NSW 2006, Australia

¹¹SETI Institute, 189 Bernardo Avenue, Mountain View, CA 94043, USA

Accepted XXX. Received YYY; in original form ZZZ

ABSTRACT

Here we present the first data release of the *Kepler* Smear Campaign, using collateral ‘smear’ data obtained by *Kepler* to reconstruct light curves of 102 stars too bright to have been otherwise observed. We describe the pipeline developed to extract and calibrate these light curves, and show that we attain photometric precision comparable to stars observed ordinarily in the nominal *Kepler* mission. In this Paper, we focus in particular on a subset of these consisting of 64 red giants for which we detect solar-like oscillations. Using high-resolution spectroscopy from the Tillinghast Reflector Échelle Spectrograph (TRES) together with asteroseismic modelling, we obtain the masses and evolutionary states of 27 of these red giant and red clump stars as benchmarks. All source code, light curves, TRES spectra, and asteroseismic and stellar parameters are publicly available as a *Kepler* legacy sample.

Key words: asteroseismology – techniques: photometric – stars: variable: general

1 INTRODUCTION

Kepler has revolutionized the field of asteroseismology for solar-like oscillations (Gilliland et al. 2010). It has yielded the first detection of gravity-mode period spacings in a red giant (Beck et al. 2011), enabling probes of interior rotation of red giants (Beck et al. 2012) and distinguishing between hydrogen- and helium-burning cores (Bedding et al. 2011). It has also permitted the determination of ages and fundamental parameters of main-sequence stars (Silva Aguirre et al. 2013), including planet-hosting stars (Huber et al. 2013; Silva Aguirre et al. 2015; Van Eylen et al. 2018), revealing the most ancient known planetary system, dating back to the earliest stages of the galaxy (Campante et al. 2015). By comparing asteroseismic stellar ages to stellar rotation periods, Angus et al. (2015) have shown that gyrochronology models cannot fit the data

with a single relation, leading van Saders et al. (2016) to suggest a qualitative change in dynamo mechanism as stars age through the main sequence.

A major outcome of the *Kepler* asteroseismology programme is a legacy sample of extremely well characterized stars that can serve as benchmarks for future work (Lund et al. 2016; Silva Aguirre et al. 2016). As well as asteroseismology, by also using optical interferometry, it has been possible to determine fundamental parameters of main-sequence and giant stars with unprecedented precision (Huber et al. 2012; White et al. 2013, 2015). Likewise by combining with spectroscopy, Hawkins et al. (2016c) have been able to produce a large sample of stars with precise elemental abundances by fitting spectroscopic data with $\log g$ and T_{eff} fixed to asteroseismically-determined values. It is necessary to calibrate such a study against benchmark stars with very precisely-determined parameters, which in practice means requires nearby bright stars that are amenable to very high signal-to-noise spectroscopy plus asteroseismology

* E-mail: benjamin.pope@nyu.edu

(Creevey et al. 2013), parallaxes (Hawkins et al. 2016a), and/or interferometry (Casagrande et al. 2014; Creevey et al. 2015). This is especially important in the context of the *Gaia* mission (Gaia Collaboration et al. 2016), which has recently put out its second data release of 1,692,919,135 sources, including 1,331,909,727 with parallaxes (Gaia Collaboration et al. 2018). These data will form the basis of many large surveys and it is vital that they are calibrated correctly. To this end, 34 FGK stars have been chosen as *Gaia*-ESO benchmark stars for which metallicities (Jofré et al. 2014), effective temperatures and surface gravities (Heiter et al. 2015), and relative abundances of α and iron-peak elements (Jofré et al. 2015) have been determined. This has been accompanied by the release of high resolution spectra (Blanco-Cuaresma et al. 2014) and formed the basis of extensions to lower metallicities (Hawkins et al. 2016b), stellar twin studies (Jofré 2016) and comparisons of stellar abundance determination pipelines (Jofré et al. 2017).

Brighter *Kepler* stars are therefore ideal benchmark targets, since photometry can be most easily complemented by *Hipparcos* parallaxes, interferometric diameters, and high resolution spectroscopy. Unfortunately, the *Kepler* field was deliberately placed to minimize overall the number of saturated stars, so that only a dozen stars brighter than 6th magnitude landed on silicon (Koch et al. 2010). This was because stars brighter than $Kp \sim 11$ saturate the CCD detector, spilling electrons up and down their column on the CCD and rendering those pixels otherwise unusable. Furthermore, due to the limited availability of bandwidth to download data from the satellite, only a fraction **What fraction?** of pixels on the *Kepler* detector are actually downloaded, these being allocated via a competitive proposal process. The result of these two target selection constraints is that photometry was obtained for only **a small number** of saturated stars in the *Kepler* field, while many bright targets were ignored. In the K2 mission (Howell et al. 2014), very saturated stars have been observed with ‘halo photometry’ using unsaturated pixels in a specially-determined region around bright stars, including the Pleiades (White et al. 2017), Aldebaran (Farr et al. 2018), and ρ Leonis (Aerts et al. 2018). Unfortunately, in the legacy *Kepler* sample, photometry of such saturated stars was rarely attempted.

Kolodziejczak & Caldwell (2011) noted a way to obtain photometry of every target on-silicon in *Kepler* using a data channel normally used for calibration, even if active pixels were not allocated and downloaded. *Kepler* employs an inter-line transfer CCD as its detector, which successively shuffles each row of pixels down to the edges of the chip to be read out. Because the *Kepler* camera lacks a shutter, the detector is exposed to light during the readout process, with the result that fluxes in each pixel are contaminated by light collected from objects in the same column. This is a particularly serious issue for faint objects in the same detector column as brighter stars, and it is important to calibrate this at each readout stage. Six rows of blank ‘masked’ pixels were allocated in each column to measure the smear bias; furthermore, six ‘virtual’ rows were recorded at the end of the readout, with the result that twelve rows of pixels sample the smear bias in each column. Kolodziejczak & Caldwell (2011) realized that these encode the light curves of bright targets in a 1D projection of the star field. The masked and virtual smear registers each receive $\sim 1/1034$ of the incident flux in each column. If this is dominated by the light from a single star, the flux combining both smear registers is equivalent to that of a star ~ 6.8 times fainter.

In Pope et al. (2016), we demonstrated a method for extracting precise light curves of bright stars in *Kepler* and K2, and presented light curves of a small number of variable stars as examples to illustrate this method. In this paper we present smear light curves of

all unobserved or significantly under-observed stars brighter than $Kp = 9$ in the *Kepler* field. This sample mostly consists of red giants and hot stars, containing only a few FG dwarfs. We find no transiting planets, but detect **M** new eclipsing binaries, and measure solar-like oscillations in 34 red giants. We do not model hot stars or FG dwarfs in great detail, but provide some discussion and initial classification of interesting variability. For eclipsing binaries, we present the results of light-curve modelling to precisely determine their parameters. For the oscillating red giants that constitute the bulk of the sample, we determine the asteroseismic parameters ν_{\max} and $\Delta\nu$, and therefore stellar masses and $\log g$ measurements; and we obtain high-resolution spectroscopy with the Tillinghast Reflector Échelle Spectrograph (TRES), from whose spectra we derive stellar parameters and elemental abundances constrained by asteroseismic parameters. We discuss the potential for these as benchmark stars for other stellar surveys, in particular *Gaia*.

We have made all new data products and software discussed in this paper publicly available, and encourage interested readers to use these in their own research.

2 METHOD

We have obtained smear light curves for our sample of red giant stars with the `keplersmear` pipeline as described in Section 2.2, performed asteroseismology on all of these to extract ν_{\max} and therefore $\log g$ as described in Section 2.3, and combined these with TRES spectra to obtain chemical abundances as described in Section 2.4.

2.1 Sample

We selected as our sample all stars on-silicon in *Kepler* with $Kp < 9$ that were targeted for fewer than 8 quarters, including those stars that were entirely unobserved. A number of these lay at the edge of a detector, with the result that in some cadences the centroid of the star did not lie on the chip; light curves from these targets were found to be of extremely low quality and all of these objects were discarded. After applying these criteria we obtained a list of 102 targets, which are listed in Table 1 in order of their *Kepler* magnitude Kp together with their spectral type from SIMBAD, *Gaia* DR2 source identifiers, apparent G magnitudes and distances from Bailer-Jones et al. (2018), the quarters for which the stars were observed, and whether spectroscopy is available as in Section 2.4 and Table 3. The *Kepler* satellite rotates between quarters, so that it cycles through four orientation ‘seasons’ each rotated from the last by 90° . Some stars did not land on silicon for all seasons: we have only one season of HD 179394; two for HD 187277, HD 226754, V554 Lyr, and BD+47 2891; and three for BD+43 3064. Aside from the restriction on stars falling on the edge of a chip like this or otherwise, the addition of our sample to the conventionally-observed stars makes the *Kepler* survey magnitude-complete down to $Kp = 9$.

In Figure 1 we show these stars on a colour-magnitude diagram in *Gaia* $Bp - Rp$ and absolute G magnitudes using *Gaia* DR2 calibrated distances from Bailer-Jones et al. (2018), and situate these in context with the entire *Kepler* sample from the `Bedell gaia-kepler.fun` crossmatch. The smear targets in this diagram appear to have not merely higher apparent brightnesses than the general *Kepler* population, but also higher intrinsic luminosities. While this could simply arise from being selected for their apparent brightness, it is worth considering whether this is because of a bias in their parallax measurements. While *Gaia* parallaxes for very bright

stars can be subject to systematic error, we have compared these to those found by *Hipparcos* (van Leeuwen 2007), and found close agreement for the brightest stars, with a scatter that increases with magnitude. We therefore suggest that parallax bias is not the reason for the smear sample sitting above the remainder of the *Kepler* sample.

We identify the evolutionary state of objects in the main sequence versus evolved stars first from the *Gaia* colour-magnitude diagram in Figure 1. Taking a cutoff in *Gaia* $B_p - R_p < 1$, we identify 64 of these objects as clearly evolved systems, and the remaining 38 lie apparently on the main sequence.

One of the main sequence objects, BD+43 3068 is a G0 dwarf with a G magnitude of 8.267944 and a distance of 53.8 ± 0.1 pc, and it is therefore surprising that it was not included in the nominal *Kepler* survey as a Solar analogue: it is possible that it was previously misidentified as a giant. Regrettably, it is only possible to reconstruct a light curve with the 30 minute long cadence and therefore it is not possible to do asteroseismology on this bright, nearby solar-like star. This light curve shows neither rotational modulation (as determined by its featureless autocorrelation) nor evidence of transits.

Considering objects lying photometrically on the main sequence, from the *Kepler* power spectrum we identify solar-like oscillations in HD 182354 and HD 176209 at frequencies consistent with them being subgiants. **Get frequencies.**

2.2 Photometry

In preparing light curves of the *Kepler* smear stars, we follow the methods described in Pope et al. (2016), with some improvements. We select using RA and Dec values from the *Kepler* Input Catalog (KIC) (Brown et al. 2011), and query MAST to find the corresponding mean pixel position for a given *Kepler* quarter. We measure the centroid of smear columns in the vicinity, and use these values to do raw aperture photometry. We find that the cosine-bell aperture used for raw photometry in Pope et al. (2016) can in some light curves introduce position-dependent systematics and jumps. We instead in this work apply a super-Gaussian aperture, $A \propto \exp \frac{-(x - x_0)^4}{w}$, where x_0 is the centroid and w a width in pixels. The very flat top of this function helps avoid significant variation with position, while still smoothly rolling off at the edges to avoid discontinuous artefacts. We calculate this on a grid of $10 \times$ subsampled points in pixel space so that the sharply varying edge changes column weights smoothly as a function of centroid. We extract photometry using apertures with a range of widths $w \in \{1.5, 2, 3, 4, 5\}$ pixels.

From this raw photometry we subtract a background light curve, which corrects for time-varying global systematics. Whereas in Pope et al. (2016) we then subtract a background estimate chosen manually, for this larger set of light curves, we now choose the lowest 25% of pixels by median flux as being unlikely to be contaminated by stars, and take our background level to be the median of this at each time sample. To denoise this, we fit a Gaussian Process with a 30-day timescale squared exponential kernel using GEORGE (Ambikasaran et al. 2015), and our final background light curve is taken to be the posterior mean of this GP.

The dominant source of residual systematic errors in nominal *Kepler* time series is a common-mode variation primarily due to thermal changes on board the spacecraft, an issue which is traditionally dealt with by identifying and fitting a linear combination of systematic modes (Twicken et al. 2010; Stumpe et al. 2012; Smith et al. 2012; Petigura & Marcy 2012). We adopt the same approach here, using the *Kepler* Pre-search Data Conditioning (PDC) Cotrending

Basis Vectors (CBVs) available from MAST, finding least-squares fits of either the first 4 or 8 CBVs to each light curve. We note that this can subtract astrophysical signals on long timescales, such that we use and recommend 4 CBV light curves for stars with variability on timescales longer than ~ 5 days, but otherwise use the 8 CBV light curves. There is some room for improvement here by simultaneously modelling astrophysical and instrumental variations, but this is beyond the scope of this paper. In the following, we will use the light curves with the lowest 6.5 hr Combined Differential Photometric Precision (CDPP) (Christiansen et al. 2012) out of all apertures, as calculated with the *k2sc* implementation (Aigrain et al. 2016). This is not necessarily the optimal choice for all red giants, especially those with oscillations on a 6.5 h timescale, but is a reasonable proxy nevertheless for white noise and leads to satisfactory results upon visual inspection of the present sample.

Because the smear data are collected along an entire CCD column, there is the risk of contamination from sufficiently bright sources. This is especially true in doing asteroseismology of red giants, where the low-amplitude stochastically-excited oscillations can be washed out in a power spectrum by the coherent high amplitude variations of a classical pulsator, even if the background star is much fainter. We can assess the importance of this contamination by considering the differences between odd and even quarters: because the *Kepler* satellite rotates 90° between successive quarters, any contaminant will lie in the same column as a smear target only every second quarter, falling in the other quarters in the same row but not necessarily the same column. We have therefore generated Lomb-Scargle periodograms (Lomb 1976; Scargle 1982) of each light curve, clipped for outliers, and considering only odd and even quarters, and visually inspected these for significant differences. In the great majority of cases they closely resemble one another, indicating that contamination is at worst a minor effect. In the case of HD 181878, a red giant, there is clear and significant contamination from a δ Scuti variable, as is seen in Figure 2.

2.3 Asteroseismology

While 64 red giants have been identified in this sample, for some of these, by visual inspection it is clear that the timescale of their variability is of the same order as a *Kepler* quarter and they are thus badly affected by systematics and systematics correction. From the 35 giants for which there is shorter-timescale variability, we have attempted to extract the asteroseismic parameters ν_{\max} and $\langle \Delta \nu \rangle$ (Kjeldsen & Bedding 1995; Chaplin & Miglio 2013). These constrain fundamental stellar parameters independently from spectroscopic or interferometric measurements:

$$\nu_{\max} \propto \frac{g}{g_{\odot}} \cdot \left(\frac{T_{\text{eff}}}{T_{\text{eff}\odot}} \right)^{\frac{1}{2}} \quad (1)$$

and

$$\langle \Delta \nu \rangle \propto \sqrt{\langle \rho \rangle} = \sqrt{\frac{M}{M_{\odot}} \left(\frac{R}{R_{\odot}} \right)^{-3}} \quad (2)$$

We follow the method of Davies & Miglio (2016), obtaining a Lomb-Scargle periodogram of the smoothed time series according to the method of García et al. (2011). We then conduct a Markov Chain Monte Carlo fit to this, applying the combined granulation and oscillation model of Kallinger et al. (2014), consisting of two

Table 1. The full set of underobserved and unobserved stars for which new light curves have been produced in this smear catalogue. Calibrated *Gaia* distances are from [Bailer-Jones et al. \(2018\)](#). Some objects, such as HD 185351, were observed in long cadence in some quarters and short cadence in others, and this is noted accordingly. The eclipsing binary V2083 Cyg was detected by *Gaia*, but a parallax could not be obtained in DR2, possibly due to binary motion. Variability classes are determined by inspection, having their usual abbreviations. EV denotes an ellipsoidal variable, but some of these could be rotation and spot modulation. γ Dor/ δ Sct denotes a γ Dor/ δ Sct hybrid, not uncertainty. H+S denotes a ‘hump and spike’ star. Question marks indicate uncertainty, and dashes – that no significant variability is observed.

Object	KIC	Spectral Type (SIMBAD)	<i>Kp</i> (mag)	<i>G</i> (mag)	<i>Gaia</i> Distance (pc)	Observed	Spectroscopy	Variability Class
HD 185351	8566020	K5	5.034	4.881522	41.2 ^{+0.1} _{-0.1}	LC:Q1-3 SC:Q16	TRES	RG
HD 186155	9163520	G5	5.055	4.923168	50.6 ^{+0.4} _{-0.4}	LC:Q1	–	EV
HD 175740	6265087	K0	5.212	5.152375	81.5 ^{+0.6} _{-0.6}	unobserved	TRES	RG
HD 184875	6954647	B0III	5.403	5.2788925	172.6 ^{+3.3} _{-3.2}	unobserved	–	EV
14 Cyg	7292420	G8.5IIbFe-0.5	5.49	5.3699827	194.3 ^{+7.0} _{-6.6}	unobserved	–	EV
HD 189178	5219588	K2	5.552	5.41016	347.3 ^{+13.0} _{-10.3}	unobserved	–	γ Dor
HD 187372	10679281	K5	5.672	5.3131795	306.4 ^{+10.3} _{-9.6}	unobserved	TRES	LPV
HD 182694	7680115	K5	5.722	5.598205	133.1 ^{+0.7} _{-0.7}	LC:Q2	TRES	RG
V380 Cyg	5385723	K5	5.771	5.6319346	1044.7 ^{+16.6} _{-95.6}	LC:Q11 SC:Q7 9 10 12-17	–	EB
HD 186121	7456762	K5	5.773	5.1762185	475.2 ^{+35.1} _{-30.7}	unobserved	TRES	LPV
HD 189684	9305008	0	5.982	5.8811946	125.2 ^{+6.2} _{-5.7}	unobserved	–	EV
HD 188252	10683303	–	6.007	5.864375	1000.6 ^{+82.6} _{-71.1}	LC:Q13	–	γ Dor
HD 181597	11555267	K5III	6.04	5.985134	135.8 ^{+0.3} _{-0.3}	unobserved	TRES	RG
HD 185286	7966681	K2	6.151	6.055302	263.5 ^{+3.9} _{-3.8}	unobserved	TRES	RG
HD 188875	5041881	K	6.164	6.091042	683.8 ^{+12.4} _{-11.9}	unobserved	TRES	RG
HD 175466	7340766	B3V	6.165	5.9186597	397.8 ^{+6.8} _{-6.6}	unobserved	–	LPV
V547 Lyr	5429948	M0	6.199	5.227579	288.9 ^{+13.1} _{-12.0}	unobserved	TRES	LPV
HD 175884	6584587	B0.5IIIn	6.21	6.144104	238.9 ^{+13.0} _{-11.4}	unobserved	TRES	RG
HD 181069	4049174	A0	6.279	6.264174	144.2 ^{+0.6} _{-0.6}	LC:Q1 10 13 14 17	TRES	RG
HD 179959	10265370	K4III	6.28	6.2575774	499.2 ^{+7.2} _{-7.0}	unobserved	TRES	RG
V543 Lyr	5429169	K5	6.299	6.159548	345.1 ^{+5.6} _{-5.5}	unobserved	–	SPB
HD 182354	2156801	B9	6.32	6.2906675	228.9 ^{+1.7} _{-1.7}	unobserved	–	RG
HD 175132	6020867	K0	6.362	6.242306	333.3 ^{+5.9} _{-5.7}	unobserved	–	EV
V819 Cyg	10618721	K0	6.381	6.243083	1114.0 ^{+70.9} _{-103.0}	LC:Q14 16 17	–	SPB
HD 183362	2715115	K0	6.394	6.2077436	571.1 ^{+18.2} _{-17.2}	unobserved	–	H+S
HD 187217	11824273	K0	6.399	6.3447323	243.2 ^{+1.8} _{-1.8}	LC:Q14-17	TRES	RG
HD 183124	8752618	K0	6.441	6.3954253	160.7 ^{+0.8} _{-0.8}	LC:Q2 4 6 8 10 12 14 16	TRES	RG
HD 190149	8262528	G5	6.488	6.1712503	409.4 ^{+3.8} _{-3.8}	unobserved	TRES	LPV
HD 181022	3946721	–	6.496	6.2475405	317.7 ^{+2.7} _{-2.7}	unobserved	TRES	LPV
HD 176582	4136285	K0	6.51	6.383207	298.6 ^{+3.9} _{-3.8}	LC:Q12-13	–	EV
HD 174177	9630812	M4-IIIa	6.575	6.4831395	223.9 ^{+1.6} _{-1.6}	unobserved	–	γ Dor
HD 180682	5177450	K5	6.617	6.5322237	295.8 ^{+1.6} _{-1.5}	LC:Q0 3 7	TRES	LPV
HD 181878	4830109	M1	6.698	6.5869	259.5 ^{+1.8} _{-1.8}	LC:Q14-17	TRES	RG
HD 174020	7800227	K2	6.753	6.6002703	433.1 ^{+4.2} _{-4.1}	LC:Q2 6 10 14	TRES	RG
HD 184787	6528001	–	6.757	6.658364	139.6 ^{+1.1} _{-1.1}	unobserved	TRES	H+S
HD 178090	6675338	A2IV	6.758	6.5490265	583.0 ^{+8.5} _{-8.3}	LC:Q1 3 10	–	LPV
HD 181681	5092997	B9	6.864	6.6958766	585.0 ^{+9.1} _{-8.9}	unobserved	TRES	RG
HD 175841	4989900	B9IIIpSi	6.885	6.797499	241.0 ^{+2.1} _{-2.1}	LC:Q11-12 14-16 SC:Q3	–	γ Dor/ δ Sct
V2083 Cyg	10342012	F5	6.902	6.81	–	unobserved	–	EB
HD 189013	10096499	K2	6.922	6.8403153	188.8 ^{+6.4} _{-6.0}	SC:Q3 gDor	–	γ Dor
HD 183203	12208512	B8	6.928	6.5295672	476.9 ^{+5.9} _{-5.8}	unobserved	TRES	LPV
HD 176626	7943968	G8II	6.933	6.84066	224.8 ^{+1.8} _{-1.7}	unobserved	–	EV
HD 181521	5180075	K0	6.939	6.8521805	217.8 ^{+3.4} _{-3.3}	unobserved	–	γ Dor/ δ Sct
HD 185397	3455268	K5	6.953	6.8550224	180.0 ^{+1.0} _{-1.0}	unobserved	–	δ Sct
HD 186255	4937492	A0	6.966	6.8618903	254.5 ^{+4.0} _{-4.0}	unobserved	–	δ Sct
HD 174829	7339102	K1III	6.967	6.9280105	355.0 ^{+3.4} _{-3.4}	unobserved	TRES	RG
V398 Lyr	4042516	G0	7.024	5.4027195	494.7 ^{+34.9} _{-30.6}	unobserved	TRES	RG
HD 181596	11910615	M3	7.05	6.862713	591.1 ^{+8.1} _{-7.8}	unobserved	TRES	RG
HD 179395	6593264	A0V	7.168	7.0700407	233.9 ^{+1.7} _{-1.7}	unobserved	–	EV
V2079 Cyg	8818020	K0	7.174	7.034088	321.5 ^{+3.7} _{-3.6}	unobserved	–	EV
HD 181328	12456737	A3	7.182	6.6139154	353.9 ^{+3.3} _{-3.3}	unobserved	TRES	LPV
HD 184483	7756961	M0	7.246	6.7187505	492.9 ^{+5.3} _{-5.4}	unobserved	TRES	LPV

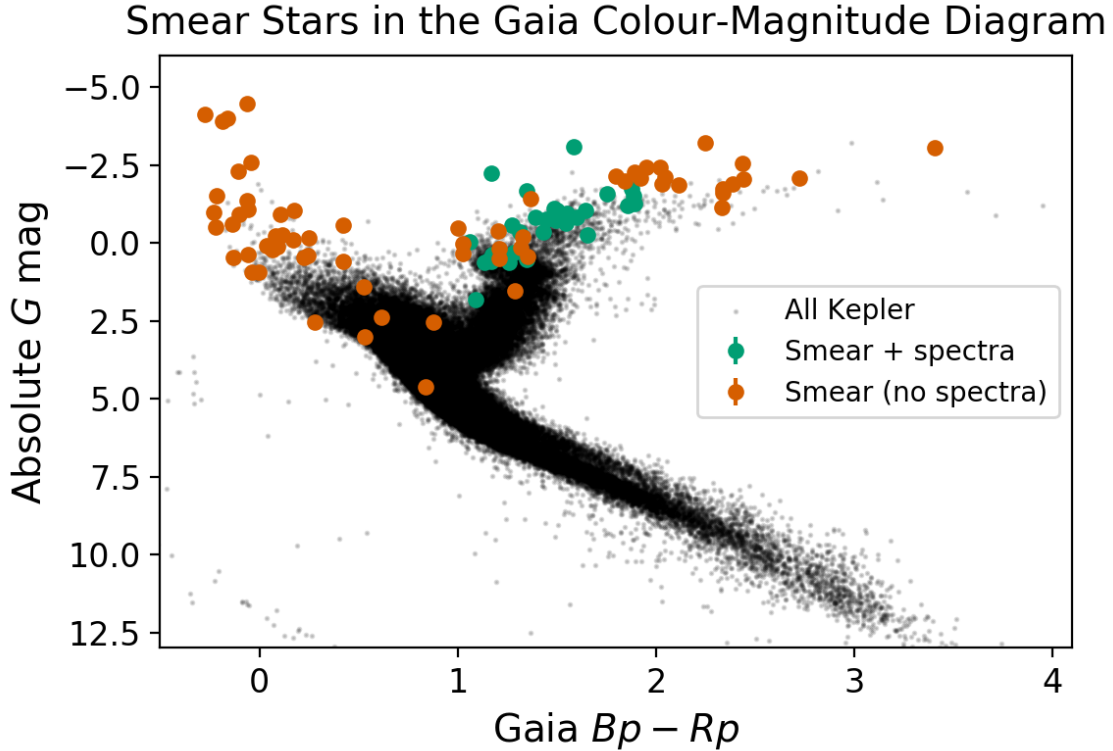


Figure 1. *Gaia* colour-magnitude diagram of the Smear Campaign stars (orange and teal) situated in sample of *Kepler* stars with *Gaia* parallax SNR > 25 (black), using the Bedell [gaia-kepler.fun](https://github.com/bedell/gaia-kepler.fun) crossmatch and *Gaia* DR2 calibrated distances from [Bailer-Jones et al. \(2018\)](https://arxiv.org/abs/201801022). The smear sample includes giants and hot main-sequence stars. Those giants for which TRES spectroscopy have been obtained are highlighted in teal. An interactive version of this diagram is available as supplementary material from the journal or at benjaminpope.github.io/data/cmd_smear.html.

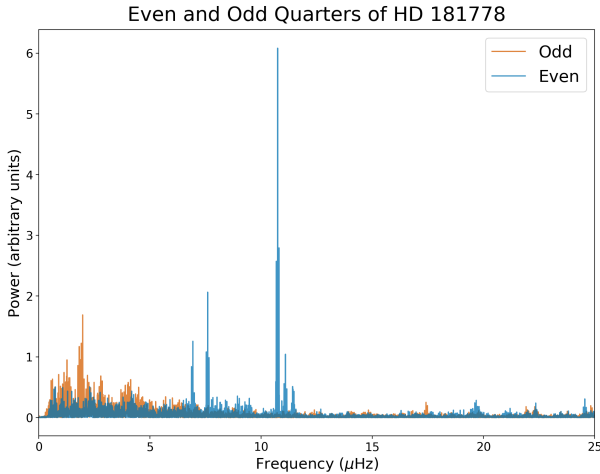


Figure 2. Power spectra of odd and even quarters of HD 181778. It is clear from inspection that while odd quarters have the power spectrum expected of a giant star, even quarters have very high amplitude coherent oscillations typical of a δ Scuti variable.

Harvey profiles for the granulation ([Harvey 1985](https://arxiv.org/abs/198501015)), a Gaussian envelope for the stellar oscillations, and a white noise background for instrumental noise. We find that the marginal posterior distribution for the Gaussian envelope is well-approximated by a single Gaussian, and take its median and standard deviation to be our estimates for ν_{\max} and its uncertainty.

To estimate $\Delta\nu$, we divide the power spectrum through by the granulation and noise models to obtain a signal-to-noise spectrum, and fit a sum of Lorentzians separated by mean large ($\Delta\nu$) and small ($\delta\nu$) separations to the part of this spectrum in the vicinity of ν_{\max} . In practice, for this dataset, $\delta\nu$ is poorly constrained, but mean $\langle\Delta\nu\rangle$ is typically well-constrained and its posterior marginal distribution is well-represented by a single Gaussian as with ν_{\max} .

We obtain good estimates of these asteroseismic parameters for 35 targets, presented in Table 2. In many of the remainder of cases, we find that the very-low-frequency ($\lesssim 2\mu\text{Hz}$) oscillations are affected by filter artefacts from detrending, and we are not able to obtain good estimates for these stars.

Once ν_{\max} has been estimated, we use the asteroseismic scaling relation for ν_{\max} (Equation 1; [Kjeldsen & Bedding 1995](https://arxiv.org/abs/199501015)) to estimate $\log g$ in order to inform extraction of chemical abundances from spectra. Using the initial spectroscopic estimate of T_{eff} , which is not significantly informed by ν_{\max} , we propagate uncertainties in ν_{\max} with Monte Carlo sampling.

For eight stars, we find that the asteroseismic fit is unsatisfactory: for BD+39 388 we cannot detect the expected oscillations; BD+43 3064 there are significant peaks but these are not consistent with the pattern expected from a red giant; for HD 179959 and HD 187217 we suspect contamination with the oscillations of a second giant, which is hard to remove from smear light curves; while for HD 188629, HD 188639 and HD 188875 we can extract a ν_{\max} but not a robust $\Delta\nu$. One star in our sample, the retired A star HD 185351, has a mode envelope that is not well fit by our model. The smear light curve for this star has already been published by [Hjørringgaard et al. \(2017\)](https://arxiv.org/abs/201701015), who showed with detailed asteroseismic

Table 1 – *continued* The full set of underobserved and unobserved stars for which new light curves have been produced in this smear catalogue. Calibrated *Gaia* distances are from [Bailer-Jones et al. \(2018\)](#).

Object	KIC	Spectral Type (SIMBAD)	<i>Kp</i> (mag)	<i>G</i> (mag)	<i>Gaia</i> Distance (pc)	Observed	Spectroscopy	Variability Class
HD 184788	6129225	A0	7.249	7.1427946	226.5 ^{+2.4} _{-2.3}	unobserved	–	?
HD 184147	9651435	A0	7.251	7.1445045	175.5 ^{+2.6} _{-2.5}	unobserved	–	EV
BD+42 3367	7447756	B5V	7.271	6.991751	762.0 ^{+15.8} _{-15.2}	unobserved	TRES	LPV
HD 177697	4994443	K5	7.3	6.7638826	472.0 ^{+5.4} _{-5.2}	unobserved	–	RG
HD 182692	10728753	M0	7.31	7.247128	226.6 ^{+1.3} _{-1.3}	unobserved	TRES	RG
HD 178797	10064283	K0	7.312	7.2491374	406.1 ^{+4.8} _{-4.7}	unobserved	TRES	RG
HD 184215	11031549	0	7.321	7.188762	361.2 ^{+6.4} _{-6.1}	unobserved	–	γ Dor
HD 188537	9110718	K0II	7.382	7.3244863	629.9 ^{+11.4} _{-11.0}	unobserved	TRES	RG
V546 Lyr	6267345	K0	7.385	6.784268	587.8 ^{+13.1} _{-12.6}	unobserved	TRES	LPV
HD 176209	9327530	B3Ve	7.437	7.3647585	282.2 ^{+2.7} _{-2.7}	unobserved	–	?
HD 174676	7420037	K0	7.481	7.4398384	993.3 ^{+26.7} _{-25.4}	unobserved	TRES	LPV
HD 186727	12316020	K2	7.499	6.9165545	581.7 ^{+9.2} _{-8.9}	unobserved	TRES	LPV
HD 181778	7816792	B8V	7.545	7.513725	374.5 ^{+3.4} _{-3.4}	unobserved	TRES	RG
HD 179394	7105221	K5	7.575	7.475068	476.2 ^{+12.2} _{-11.6}	unobserved	TRES	–
HD 187277	6967644	K0	7.579	7.4642863	96.9 ^{+0.4} _{-0.4}	unobserved	–	–
HD 186994	8766240	K2	7.585	7.4506955	1866.1 ^{+138.1} _{-120.6}	unobserved	–	EB
HD 183383	6777469	M3III	7.64	7.5365596	357.1 ^{+5.5} _{-5.3}	unobserved	–	EV
HD 180475	11656042	A3	7.664	7.5950294	546.1 ^{+8.0} _{-7.8}	unobserved	TRES	RG
BD+42 3393	6870455	M1III	7.664	7.4138913	929.0 ^{+25.9} _{-24.5}	unobserved	TRES	LPV
HD 185117	9094435	B9	7.696	7.472238	817.7 ^{+14.8} _{-14.3}	unobserved	–	LPV
HD 176894	6267965	M0II–III	7.7	7.6103888	82.8 ^{+0.2} _{-0.2}	unobserved	–	γ Dor
HD 188629	8710324	K0	7.743	7.5462255	651.0 ^{+12.0} _{-11.6}	unobserved	TRES	LPV
HD 177781	2970780	B5V	7.744	7.700899	296.2 ^{+2.6} _{-2.5}	unobserved	–	γ Dor/ δ Sct
HD 182737	1572070	K0	7.82	7.757723	460.3 ^{+6.7} _{-6.5}	unobserved	–	LPV
HD 226754	6234579	0	7.829	7.702354	391.8 ^{+6.1} _{-5.9}	unobserved	TRES	RG
HD 178910	11288450	G5	7.864	7.8481197	291.3 ^{+5.4} _{-5.4}	unobserved	TRES	RG
HD 181097	4149233	A5	7.92	7.8478937	434.3 ^{+6.2} _{-6.0}	unobserved	TRES	RG
HD 180658	6195870	A2	7.932	7.870914	282.2 ^{+2.3} _{-2.3}	unobserved	TRES	RG
HD 182531	11188366	B9IV	7.955	7.8590217	599.3 ^{+9.2} _{-8.9}	unobserved	TRES	RG
BD+48 2955	10988024	K2	7.961	7.8992686	589.4 ^{+11.6} _{-11.1}	unobserved	TRES	RG
HD 180312	4551179	A2	7.97	7.8340764	290.5 ^{+2.4} _{-2.4}	unobserved	TRES	RG
HD 184565	6047321	K0	7.972	7.9430523	380.9 ^{+4.3} _{-4.3}	unobserved	–	LPV
HD 181880	3337423	M5	7.982	7.940268	541.2 ^{+10.1} _{-9.7}	unobserved	TRES	RG
HD 179396	3838362	K5	8.001	7.9701843	321.2 ^{+2.7} _{-2.6}	unobserved	TRES	RG
HD 185524	8960196	F0	8.022	7.9525204	753.4 ^{+15.9} _{-15.2}	unobserved	TRES	LPV
HD 189636A	10298067	–	8.025	8.118049	384.7 ^{+6.0} _{-5.8}	unobserved	–	?
HD 189750	8521828	K5	8.052	8.060998	327.0 ^{+3.8} _{-3.8}	unobserved	–	?
HD 189636B	10298061	K0	8.107	8.023957	376.4 ^{+4.9} _{-4.7}	unobserved	–	?
BD+36 3564	1575741	F5II–III	8.128	8.040623	547.1 ^{+11.6} _{-11.1}	unobserved	TRES	RG
BD+39 3577	4989821	G8III	8.131	8.089526	311.7 ^{+2.7} _{-2.7}	unobserved	TRES	RG
V554 Lyr	5001462	K0	8.179	8.092074	335.7 ^{+4.6} _{-4.5}	unobserved	–	α^2 CVn
BD+47 2825	10337574	B2III	8.251	8.236473	485.8 ^{+7.3} _{-7.1}	unobserved	–	EB
BD+39 3882	4850372	A2V	8.259	8.158849	143.3 ^{+0.7} _{-0.7}	unobserved	–	Irregular
BD+43 3064	8075287	G7IIIa	8.284	8.20331	641.0 ^{+20.3} _{-19.1}	unobserved	TRES	RG
BD+43 3068	8006792	B1.1III+B2.5/3V:	8.308	8.267944	53.8 ^{+0.1} _{-0.1}	unobserved	–	–
BD+43 3213	7747499	A5III	8.311	8.13925	948.8 ^{+25.8} _{-24.5}	unobserved	TRES	LPV
BD+42 3150	7091342	B9III	8.35	8.31532	546.0 ^{+32.5} _{-29.1}	unobserved	–	?
BD+43 3171	7810954	M3III	8.373	8.178079	751.5 ^{+17.2} _{-16.5}	unobserved	TRES	LPV
BD+48 2904	11085556	K5	8.487	8.439092	400.9 ^{+5.4} _{-5.3}	unobserved	–	RG
BD+47 2891	10347606	K1III	8.68	8.6254015	262.8 ^{+1.7} _{-1.6}	unobserved	–	RG

modelling that it had a zero-age main sequence mass of $\sim 1.60M_{\odot}$ and used it to calibrate the convective overshoot parameter for low-luminosity red giants. The bulk asteroseismic modelling presented here should therefore be considered to be superseded by the more detailed model of [Hj rtinggaard et al. \(2017\)](#).

2.4 Spectroscopy

For the whole red giant sample, we have obtained high-resolution spectroscopy with TRES in order to constrain stellar parameters and elemental abundances. Operating with spectral resolving power $R = 44000$, we obtain signal-to-noise ratios of tens to hundreds per resolution element. We note that this resolution and SNR are

Table 2. Bulk asteroseismic parameters $\Delta\nu$, ν_{\max} , and ϵ for the red giant sample as discussed in Section 2.3.

Object	$\Delta\nu$ (μHz)	ν_{\max} (μHz)	ϵ
BD+36 3564	0.95 ± 0.03	5.08 ± 0.10	0.83 ± 0.20
BD+39 3577	1.68 ± 0.01	13.27 ± 0.32	0.74 ± 0.06
BD+42 3150	4.22 ± 0.03	38.32 ± 0.96	0.70 ± 0.07
BD+43 3171	0.42 ± 0.05	1.98 ± 0.05	0.80 ± 0.17
BD+43 3213	0.49 ± 0.01	2.56 ± 0.06	1.01 ± 0.07
BD+48 2904	2.85 ± 0.01	23.13 ± 0.72	0.86 ± 0.08
BD+48 2955	0.90 ± 0.01	5.44 ± 0.08	0.81 ± 0.05
HD 174020	0.56 ± 0.02	2.48 ± 0.10	0.89 ± 0.08
HD 174829	1.28 ± 0.01	7.95 ± 0.16	0.78 ± 0.06
HD 175740	5.93 ± 0.01	64.33 ± 0.78	1.00 ± 0.02
HD 175884	1.12 ± 0.01	7.07 ± 0.11	0.96 ± 0.08
HD 176209	4.22 ± 0.08	36.08 ± 0.77	0.87 ± 0.06
HD 178797	1.03 ± 0.02	6.34 ± 0.09	0.74 ± 0.29
HD 178910	3.64 ± 0.02	32.06 ± 0.31	0.83 ± 0.05
HD 179396	3.76 ± 0.02	31.02 ± 0.44	0.92 ± 0.03
HD 180312	4.17 ± 0.02	33.84 ± 0.28	0.96 ± 0.04
HD 180475	0.82 ± 0.00	4.34 ± 0.10	0.68 ± 0.03
HD 180658	4.00 ± 0.02	33.76 ± 0.50	0.90 ± 0.05
HD 180682	0.77 ± 0.05	3.68 ± 0.08	1.07 ± 0.15
HD 181022	0.38 ± 0.01	1.58 ± 0.03	0.70 ± 0.10
HD 181069	4.43 ± 0.01	41.46 ± 0.32	0.90 ± 0.02
HD 181097	1.61 ± 0.02	11.16 ± 0.14	0.72 ± 0.36
HD 181597	3.11 ± 0.01	25.84 ± 0.25	0.97 ± 0.02
HD 181778	2.56 ± 0.02	22.86 ± 0.29	0.72 ± 0.06
HD 181880	1.04 ± 0.01	6.54 ± 0.10	0.76 ± 0.05
HD 182354	2.66 ± 0.01	24.73 ± 0.37	0.74 ± 0.04
HD 182531	1.03 ± 0.00	6.47 ± 0.09	0.86 ± 0.03
HD 182692	4.66 ± 0.01	44.38 ± 0.47	0.87 ± 0.02
HD 182694	5.71 ± 0.01	69.78 ± 1.02	0.94 ± 0.25
HD 183124	4.39 ± 0.01	39.59 ± 0.29	0.95 ± 0.03
HD 185286	0.72 ± 0.01	4.23 ± 0.10	0.73 ± 0.08
HD 188537	1.55 ± 0.01	13.40 ± 0.34	0.72 ± 0.07
HD 189636	2.91 ± 0.01	25.97 ± 0.74	0.97 ± 0.04
HD 189750	4.16 ± 0.04	36.14 ± 0.58	0.94 ± 0.08
HD 226754	1.19 ± 0.01	7.41 ± 0.19	0.74 ± 0.08

sufficient for an exploratory study, but for more detailed analysis it will be desirable to use APOGEE or similar instruments at higher resolution and SNR. From this observing run we have 35 unique targets with seismic $\log g$ and spectra, one more star than the *Gaia*-ESO benchmark set and a significant addition to the ensemble of bright red giants with asteroseismic parameter determinations. These are unfortunately not the same 35 unique targets as for the asteroseismic analysis presented above in Section 2.3: due to observing constraints, we were unable to obtain spectra for BD+42 315, BD+48 290, HD 176209, HD 182354, HD 189636, or HD 189750.

To derive stellar parameters from our TRES spectra, we initially run the Stellar Parameter Classification (SPC; Buchhave et al. 2012) code to determine T_{eff} and $\log g$, using the SPC T_{eff} to inform the asteroseismic estimation of $\log g$ from ν_{\max} . For deriving abundances, T_{eff} is fixed from the results of an initial SPC fit, while $\log g$ is fixed to the seismic values. The other stellar atmospheric parameters including the microturbulent velocity (v_{mic}), and broadening (convolution by V_{mac} , $v_{\text{sin } i}$ and the instrumental line profile) as well as [Fe/H] and chemical abundances for 20 chemical species are derived using the Brussels Automatic Code for Characterizing High accuracy Spectra (BACCHUS; Masseron et al. 2016), and the results from this calculation are displayed in Table 3. BAC-

CHUS uses an interpolation scheme through a grid of MARCS model atmospheres (Gustafsson et al. 2008) in combination with TURBOSPECTRUM (Alvarez & Plez 1998; Plez 2012). For the calculation of synthetic spectra, atomic line information has been taken from the fifth version of the *Gaia*-ESO linelist (Heiter et al., in preparation). Additionally we used the molecular species for CH (Masseron et al. 2014), CN, NH, OH, MgH C₂ (T. Masseron, private communication). The SiH molecular information is adopted from the Kurucz linelists and the information for TiO, ZrO, FeH, CaH from B. Plez (private communication).

Individual elemental abundances are derived by first fixing the stellar atmospheric parameters to those determined above. Spectra are then synthesized in regions centered around an absorption feature of the element we want to derive. The spectra generated will have different [X/Fe] values. A χ^2 minimization procedure is then done to derive the best fitting abundance for each line. The reported abundances are the median [X/Fe] value of the various line regions for a given element. To achieve the most precise abundances we have derived them using both with and without a line-by-line differential approach with respect to Arcturus (α Boötis) using the method described by Jofré et al. (2015) and the Arcturus abundances from (Hawkins et al. 2016c). The results of these absolute abundance calculations **without the line-by-line differential analysis implemented?**, are presented in Tables 4, 5 and 6. Because for most elements Arcturus differential abundances are not available, these are provided as supplementary online-only material. No abundances for oxygen could be reliably derived for any of the stars in our spectroscopic sample by either method.

3 RESULTS

3.1 Red Giants

3.1.1 Chemical Composition

place [X/Fe] vs [Fe/H] diagrams here and discuss which Galactic populations these stars come from. May also want to discuss how these span the typical Galactic populations and can act as benchmark stars for APOGEE or other large surveys

Two of the stars in our sample also appear in the Hypatia catalogue of stellar abundances (Hinkel et al. 2014): HD 185351 and HD 175740. The abundances reported here for HD 185351 are consistent within the large errorbars of both surveys with those reported in Hypatia, while for HD 175740 they are not. **Keith - what's going on here? Check this?**

3.1.2 Red Clump Stars

Red clump stars, which burn helium in their cores, differ significantly in their core structure from stars on the hydrogen shell burning red giant sequence. They can therefore be distinguished from hydrogen-shell burning giants asteroseismologically, due to their much higher g -mode period spacings (Bedding et al. 2011). The moniker ‘red clump’ arises from the fact that such stars can have a very narrow range of luminosities, so that they appear as a clump in the HR diagram (Girardi 2016). This property makes them useful standard candles to which distances can be accurately computed from photometry. Red clump stars have been used to calibrate the *Gaia* survey’s parallaxes at long distances (Davies et al. 2017; Hawkins et al. 2017; Ruiz-Dern et al. 2018). *Gaia* DR2 parallaxes have a zero-point offset of ~ 0.03 mas (Lindgren et al. 2018), and in particular hierarchical models of the ensemble of *Gaia* clump

Table 3. Fundamental stellar parameters for the red giant sample as determined jointly by asteroseismology (asteroseismic $\log g$; Section 2.3) and spectroscopy (RV, T_{eff} , $\log g$, [M/H], $V \sin i$, and SNR; Section 2.4.)

Object	RV (km/s)	T_{eff} (K)	$\log g$	[M/H]	$V \sin i$ (km/s)	SNR
BD+36 3564	-77.84 ± 0.05	4301 ± 50	1.58 ± 0.01	-0.34 ± 0.08	5.14 ± 0.50	71.8
BD+39 3577	-14.81 ± 0.07	5079 ± 50	2.03 ± 0.01	-0.11 ± 0.08	3.98 ± 0.50	92.8
BD+43 3171	-16.32 ± 0.11	4072 ± 50	1.16 ± 0.01	-0.17 ± 0.08	5.68 ± 0.50	68.6
BD+43 3213	-14.16 ± 0.16	4131 ± 50	1.27 ± 0.01	0.07 ± 0.08	6.24 ± 0.50	57.3
BD+48 2955	1.66 ± 0.04	4344 ± 50	1.61 ± 0.01	-0.32 ± 0.08	4.78 ± 0.50	31.7
HD 174020	-14.84 ± 0.08	4162 ± 50	1.26 ± 0.02	-0.10 ± 0.08	5.81 ± 0.50	120.1
HD 174829	10.15 ± 0.03	4482 ± 50	1.78 ± 0.01	-0.40 ± 0.08	4.41 ± 0.50	112.2
HD 175740	-8.82 ± 0.05	4973 ± 50	2.71 ± 0.01	-0.05 ± 0.08	3.66 ± 0.50	264.0
HD 175740	-8.82 ± 0.05	4973 ± 50	2.71 ± 0.01	-0.05 ± 0.08	3.66 ± 0.50	264.0
HD 175740	-8.82 ± 0.05	4973 ± 50	2.71 ± 0.01	-0.05 ± 0.08	3.66 ± 0.50	264.0
HD 175740	-8.82 ± 0.05	4973 ± 50	2.71 ± 0.01	-0.05 ± 0.08	3.66 ± 0.50	264.0
HD 175740	-8.82 ± 0.05	4973 ± 50	2.71 ± 0.01	-0.05 ± 0.08	3.66 ± 0.50	264.0
HD 175884	-34.39 ± 0.07	4466 ± 50	1.73 ± 0.01	-0.27 ± 0.08	4.46 ± 0.50	144.4
HD 178797	6.35 ± 0.05	4406 ± 50	1.68 ± 0.01	-0.37 ± 0.08	4.18 ± 0.50	77.1
HD 178910	-14.28 ± 0.05	4589 ± 50	2.39 ± 0.00	0.14 ± 0.08	4.26 ± 0.50	76.9
HD 179396	24.80 ± 0.04	4781 ± 50	2.39 ± 0.01	-0.21 ± 0.08	3.99 ± 0.50	82.7
HD 180312	-21.94 ± 0.05	4916 ± 50	2.43 ± 0.00	-0.44 ± 0.08	4.05 ± 0.50	73.5
HD 180312	-21.94 ± 0.05	4916 ± 50	2.43 ± 0.00	-0.44 ± 0.08	4.05 ± 0.50	73.5
HD 180475	-45.90 ± 0.08	4398 ± 50	1.52 ± 0.01	-0.44 ± 0.08	4.39 ± 0.50	58.4
HD 180658	2.97 ± 0.06	4802 ± 50	2.43 ± 0.01	-0.12 ± 0.08	3.81 ± 0.50	72.3
HD 180682	30.99 ± 0.07	4410 ± 50	1.45 ± 0.01	-0.51 ± 0.08	4.88 ± 0.50	80.1
HD 181022	-80.39 ± 0.16	4045 ± 50	1.06 ± 0.01	-0.28 ± 0.08	5.75 ± 0.50	108.8
HD 181069	9.99 ± 0.05	4842 ± 50	2.52 ± 0.00	-0.05 ± 0.08	3.53 ± 0.50	90.0
HD 181097	-5.60 ± 0.08	4520 ± 50	1.93 ± 0.01	-0.28 ± 0.08	4.08 ± 0.50	69.7
HD 181597	-13.06 ± 0.04	4751 ± 50	2.31 ± 0.00	-0.23 ± 0.08	2.23 ± 0.50	161.8
HD 181778	-22.04 ± 0.06	4664 ± 50	2.25 ± 0.01	-0.19 ± 0.08	4.23 ± 0.50	87.6
HD 181880	0.56 ± 0.08	4405 ± 50	1.70 ± 0.01	-0.30 ± 0.08	4.44 ± 0.50	71.2
HD 182531	-7.34 ± 0.05	4413 ± 50	1.69 ± 0.01	-0.24 ± 0.08	4.39 ± 0.50	71.4
HD 182692	-8.01 ± 0.05	4965 ± 50	2.55 ± 0.00	0.09 ± 0.08	3.40 ± 0.50	72.8
HD 182694	-0.87 ± 0.06	5178 ± 50	2.76 ± 0.01	-0.12 ± 0.08	5.12 ± 0.50	187.2
HD 183124	14.96 ± 0.01	4911 ± 50	2.50 ± 0.00	-0.15 ± 0.08	5.19 ± 0.50	114.3
HD 185286	-13.70 ± 0.08	4301 ± 50	1.50 ± 0.01	-0.14 ± 0.08	5.16 ± 0.50	135.6
HD 188537	-18.03 ± 0.15	4961 ± 50	2.03 ± 0.01	-0.08 ± 0.08	10.68 ± 0.50	67.0
HD 226754	18.66 ± 0.10	4370 ± 50	1.75 ± 0.01	0.08 ± 0.08	4.78 ± 0.50	62.5

stars can be used to accurately estimate this and thereby improve the accuracy of *Gaia* distances greater than a few kpc (Hawkins et al., in prep.).

From visual inspection of the power spectra, HD 181069, HD 183124, HD 182354, HD 182692, and HD 180658 are seen to be red clump stars. A power spectrum of the best example of these, HD 183124, together with an échelle diagram used to estimate its g -mode period spacing, is shown in Figure 3. While precise characterization of these stars to the necessary degree is beyond the scope of this paper, they are ideal candidates for anchoring models of the mass and metallicity dependence of red clump properties for calibrating *Gaia* and other distance measures.

3.2 Main Sequence Stars

For all the main sequence stars in our sample, we visually inspected light curves and power spectra to determine their variability class. In the following subsections, we will briefly comment on some of the findings. As main sequence variables are so diverse, and suited to varied science cases, we have attempted only a very preliminary study of these stars in this paper, leaving detailed analysis to future work.

3.2.1 Classical Pulsators

The sample contains many δ Sct and γ Dor variables, and several hybrid pulsators. [Simon - add text here](#). Including hotter stars, we also detect SPB pulsations in [some stars - Conny/Tim van Reeth?](#).

3.2.2 Hump and Spike Stars

Two stars in the sample show the ‘hump-and-spike’ morphology in their power spectra (a broad ‘hump’ of low-amplitude oscillations dominated by one high amplitude coherent oscillation): HD 186155 (HR 7495), and HD 183362 (HR 7403), respectively the third brightest and 37th-brightest stars on silicon and the brightest two stars that show this effect. [Saio et al. \(2018\)](#) have recently claimed the hump-and-spike power spectra as evidence for Rossby modes. The F5 star HD 186155, identified by SIMBAD as having a giant spectral type of F5II-III, is shown by its *Gaia* distance to in fact lie on the main sequence. The other example is the B3e star HD 183362 at $G = -2.576$. A detailed study of these stars will be presented by Antoci et al., in prep.

Another star with a hump-and-spike spectrum is Boyajian’s Star, which shows deep enigmatic dips in brightness ([Boyajian et al. 2016](#)), and has faded both throughout the *Kepler* mission

Table 4. Chemical abundances relative to iron for stars in the red giant sample as determined by BACCHUS, without differential line-by-line comparison to Arcturus, as described in Section 2.4, for the elements Ca, Mg, Si, Ti, Al, Ba, and Na. Dashes indicate elements for which abundances could not be reliably computed. The catalogue of abundances for more elements continues in Tables 5 and 6.

Object	[Ca/Fe]	[Mg/Fe]	[Si/Fe]	[Ti/Fe]	[Al/Fe]	[Ba/Fe]	[Na/Fe]
BD+36 3564	0.21 ± 0.02	0.33 ± 0.03	0.10 ± 0.03	0.34 ± 0.04	0.40 ± 0.01	–	0.26 ± 0.08
BD+39 3577	0.13 ± 0.02	0.22 ± 0.04	−0.11 ± 0.02	0.08 ± 0.04	0.21 ± 0.01	0.35 ± 0.10	0.42 ± 0.00
BD+43 3064	0.19 ± 0.04	0.21 ± 0.03	−0.01 ± 0.03	0.28 ± 0.04	0.36 ± 0.01	–	0.48 ± 0.06
BD+43 3171	0.29 ± 0.03	0.26 ± 0.06	−0.00 ± 0.07	0.21 ± 0.06	0.42 ± 0.01	0.33 ± 0.18	0.18 ± 0.25
BD+43 3213	0.19 ± 0.03	0.23 ± 0.07	−0.18 ± 0.11	0.27 ± 0.07	0.37 ± 0.04	–	0.62 ± 0.37
BD+48 2955	0.22 ± 0.05	0.20 ± 0.03	0.08 ± 0.04	0.30 ± 0.04	0.30 ± 0.07	–	0.23 ± 0.14
HD 174020	0.33 ± 0.03	0.23 ± 0.04	−0.07 ± 0.06	0.29 ± 0.07	0.39 ± 0.03	–	0.26 ± 0.33
HD 174829	0.16 ± 0.04	0.20 ± 0.06	0.05 ± 0.05	0.19 ± 0.03	0.29 ± 0.01	–	0.31 ± 0.04
HD 175740	0.12 ± 0.02	0.07 ± 0.05	−0.05 ± 0.02	0.14 ± 0.03	0.21 ± 0.01	0.30 ± 0.07	0.34 ± 0.03
HD 175884	0.23 ± 0.02	0.20 ± 0.03	−0.01 ± 0.03	0.32 ± 0.03	0.34 ± 0.01	–	0.46 ± 0.06
HD 178797	0.22 ± 0.02	0.32 ± 0.03	0.06 ± 0.03	0.40 ± 0.04	0.42 ± 0.01	0.39 ± 0.22	0.45 ± 0.03
HD 178910	0.20 ± 0.03	0.20 ± 0.03	0.15 ± 0.05	0.20 ± 0.03	0.39 ± 0.04	0.25 ± 0.08	0.36 ± 0.98
HD 179396	0.09 ± 0.02	0.19 ± 0.03	0.04 ± 0.05	0.13 ± 0.02	0.27 ± 0.02	0.31 ± 0.03	0.28 ± 0.04
HD 179959	0.04 ± 0.04	0.06 ± 0.04	0.01 ± 0.03	0.03 ± 0.03	0.15 ± 0.02	–	0.38 ± 0.02
HD 180312	0.09 ± 0.02	0.21 ± 0.03	0.06 ± 0.03	0.09 ± 0.03	0.31 ± 0.01	0.37 ± 0.08	0.19 ± 0.01
HD 180475	0.23 ± 0.03	0.33 ± 0.03	0.03 ± 0.01	0.36 ± 0.04	0.41 ± 0.02	0.30 ± 0.20	0.40 ± 0.03
HD 180658	0.15 ± 0.03	0.19 ± 0.04	−0.01 ± 0.03	0.21 ± 0.03	0.35 ± 0.01	0.21 ± 0.09	0.39 ± 0.04
HD 180682	0.25 ± 0.02	0.45 ± 0.03	0.13 ± 0.02	0.47 ± 0.04	0.51 ± 0.05	0.19 ± 0.05	0.32 ± 0.01
HD 181022	0.34 ± 0.02	0.34 ± 0.06	0.01 ± 0.08	0.49 ± 0.06	–	0.31 ± 0.23	0.09 ± 0.48
HD 181069	0.13 ± 0.02	0.17 ± 0.04	−0.03 ± 0.05	0.19 ± 0.03	0.28 ± 0.02	0.26 ± 0.09	0.45 ± 0.06
HD 181097	0.25 ± 0.02	0.27 ± 0.03	−0.02 ± 0.03	0.35 ± 0.03	0.34 ± 0.02	–	0.46 ± 0.06
HD 181597	0.19 ± 0.02	0.20 ± 0.05	−0.03 ± 0.02	0.27 ± 0.04	0.28 ± 0.00	0.28 ± 0.05	0.42 ± 0.04
HD 181778	0.06 ± 0.03	0.12 ± 0.03	0.00 ± 0.03	0.09 ± 0.03	0.28 ± 0.02	0.47 ± 0.05	0.42 ± 0.12
HD 181880	0.26 ± 0.02	0.30 ± 0.03	0.06 ± 0.04	0.35 ± 0.03	0.42 ± 0.01	–	0.40 ± 0.05
HD 182531	0.22 ± 0.02	0.21 ± 0.05	−0.07 ± 0.03	0.37 ± 0.04	0.39 ± 0.01	–	0.48 ± 0.06
HD 182692	0.19 ± 0.03	0.18 ± 0.04	−0.12 ± 0.03	0.22 ± 0.04	0.35 ± 0.03	0.13 ± 0.05	0.38 ± 0.12
HD 182694	0.10 ± 0.02	0.11 ± 0.04	−0.04 ± 0.02	0.05 ± 0.02	0.14 ± 0.01	–	0.32 ± 0.01
HD 183124	0.17 ± 0.02	0.21 ± 0.04	−0.02 ± 0.04	0.19 ± 0.03	0.29 ± 0.00	0.25 ± 0.05	0.35 ± 0.02
HD 185286	0.34 ± 0.02	0.22 ± 0.04	−0.04 ± 0.04	0.40 ± 0.06	0.42 ± 0.02	–	0.55 ± 0.53
HD 185351	0.13 ± 0.03	0.08 ± 0.05	−0.08 ± 0.02	0.20 ± 0.03	0.22 ± 0.00	0.21 ± 0.09	0.38 ± 0.01
HD 187217	0.16 ± 0.04	0.28 ± 0.02	−0.09 ± 0.03	0.14 ± 0.04	0.32 ± 0.03	0.21 ± 0.14	–
HD 188537	0.11 ± 0.04	0.27 ± 0.04	0.02 ± 0.03	0.11 ± 0.04	0.25 ± 0.05	0.24 ± 0.07	–
HD 188629	0.30 ± 0.03	0.21 ± 0.03	−0.04 ± 0.07	0.37 ± 0.07	0.41 ± 0.04	–	0.46 ± 0.32
HD 188875	0.18 ± 0.04	0.22 ± 0.03	−0.07 ± 0.03	0.29 ± 0.04	0.33 ± 0.02	–	0.61 ± 1.09
HD 226754	0.30 ± 0.02	0.31 ± 0.04	0.03 ± 0.04	0.40 ± 0.06	0.48 ± 0.07	0.43 ± 0.00	0.47 ± 0.18

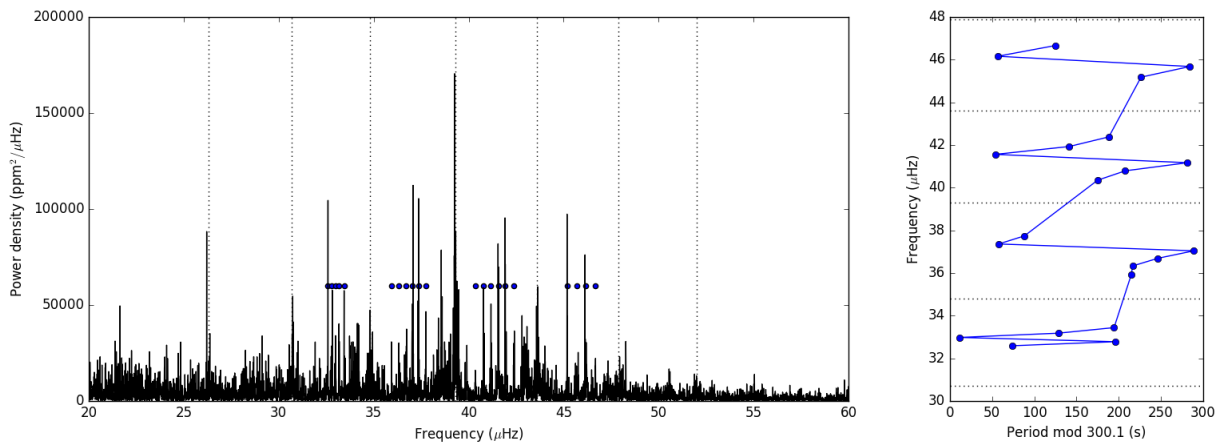


Figure 3. Power spectrum (left) and échelle diagram (right) of the solar-like oscillations of the red clump star HD 183124. The modes in the power spectrum used for the échelle diagram are highlighted with blue dots. In the échelle diagram we see the characteristic pattern of ‘bumped’ modes from avoided crossings between the comb of p -modes and g -mode oscillations with a period spacing of $\Delta\Pi = 300.1$ s.

Table 5. Chemical abundances relative to iron for stars in the red giant sample as determined by BACCHUS, without differential line-by-line comparison to Arcturus, as described in Section 2.4, for the elements Ni, Mn, Co, Eu, La, Zr, and Sr. Dashes indicate elements for which abundances could not be reliably computed. The catalogue of abundances for more elements continues in Table 6.

Object	[Ni/Fe]	[Mn/Fe]	[Co/Fe]	[Eu/Fe]	[La/Fe]	[Zr/Fe]	[Sr/Fe]
BD+36 3564	0.01 ± 0.04	0.08 ± 0.00	0.13 ± 0.02	0.25 ± 0.03	−0.02 ± 0.07	0.10 ± 0.02	0.34 ± 0.12
BD+39 3577	−0.05 ± 0.03	−0.03 ± 0.06	−0.02 ± 0.02	−0.22 ± 0.04	−0.25 ± 0.02	0.13 ± 0.08	–
BD+43 3064	0.05 ± 0.04	0.21 ± 0.02	0.13 ± 0.02	0.28 ± 0.06	0.15 ± 0.02	0.32 ± 0.04	0.25 ± 0.12
BD+43 3171	0.04 ± 0.05	0.11 ± 0.09	0.14 ± 0.05	0.21 ± 0.05	−0.06 ± 0.11	0.36 ± 0.07	–
BD+43 3213	0.06 ± 0.10	0.33 ± 0.07	0.03 ± 0.05	0.06 ± 0.04	−0.11 ± 0.05	0.49 ± 0.11	0.64 ± 0.47
BD+48 2955	0.05 ± 0.04	0.10 ± 0.02	0.12 ± 0.04	0.28 ± 0.04	0.24 ± 0.05	0.34 ± 0.05	–
HD 174020	0.05 ± 0.05	0.23 ± 0.02	0.10 ± 0.04	0.11 ± 0.04	0.02 ± 0.07	–	0.37 ± 0.89
HD 174829	−0.06 ± 0.04	−0.02 ± 0.07	0.05 ± 0.02	0.15 ± 0.01	0.12 ± 0.05	0.08 ± 0.03	–
HD 175740	0.03 ± 0.04	0.06 ± 0.01	0.08 ± 0.02	0.09 ± 0.07	0.12 ± 0.01	0.18 ± 0.02	–
HD 175884	0.04 ± 0.05	0.14 ± 0.02	0.10 ± 0.02	0.19 ± 0.02	0.14 ± 0.03	0.26 ± 0.02	–
HD 178797	0.05 ± 0.04	0.13 ± 0.11	0.18 ± 0.03	0.26 ± 0.02	0.14 ± 0.02	0.23 ± 0.03	–
HD 178910	0.28 ± 0.07	0.21 ± 0.05	0.17 ± 0.03	−0.02 ± 0.06	−0.13 ± 0.06	0.00 ± 0.03	–
HD 179396	−0.02 ± 0.04	0.09 ± 0.02	0.08 ± 0.03	−0.05 ± 0.03	0.05 ± 0.03	0.04 ± 0.02	–
HD 179959	−0.08 ± 0.04	−0.15 ± 0.04	−0.05 ± 0.02	0.16 ± 0.06	0.18 ± 0.01	0.14 ± 0.07	–
HD 180312	0.02 ± 0.03	−0.09 ± 0.03	0.07 ± 0.01	0.34 ± 0.05	0.04 ± 0.07	0.08 ± 0.02	–
HD 180475	0.03 ± 0.05	0.16 ± 0.04	0.19 ± 0.02	0.19 ± 0.07	0.18 ± 0.03	0.25 ± 0.03	–
HD 180658	0.03 ± 0.06	0.13 ± 0.03	0.11 ± 0.02	–	0.04 ± 0.04	0.16 ± 0.07	–
HD 180682	0.06 ± 0.04	−0.03 ± 0.08	0.20 ± 0.02	0.26 ± 0.03	−0.03 ± 0.02	0.22 ± 0.03	–
HD 181022	0.02 ± 0.07	0.05 ± 0.11	0.14 ± 0.05	0.26 ± 0.03	−0.03 ± 0.21	0.36 ± 0.14	–
HD 181069	0.08 ± 0.05	0.16 ± 0.03	0.12 ± 0.02	0.09 ± 0.03	0.02 ± 0.04	0.10 ± 0.03	–
HD 181097	0.01 ± 0.04	0.02 ± 0.11	0.14 ± 0.03	0.28 ± 0.04	0.17 ± 0.02	0.23 ± 0.03	–
HD 181597	0.03 ± 0.04	0.14 ± 0.01	0.13 ± 0.02	0.18 ± 0.03	0.13 ± 0.01	0.26 ± 0.03	–
HD 181778	−0.00 ± 0.05	0.13 ± 0.02	0.04 ± 0.02	0.16 ± 0.01	0.08 ± 0.03	0.11 ± 0.03	–
HD 181880	0.04 ± 0.04	0.10 ± 0.01	0.18 ± 0.03	0.32 ± 0.04	0.17 ± 0.02	0.33 ± 0.04	–
HD 182531	0.06 ± 0.04	0.17 ± 0.06	0.11 ± 0.02	0.16 ± 0.05	0.15 ± 0.03	0.36 ± 0.03	0.35 ± 0.14
HD 182692	0.03 ± 0.05	0.22 ± 0.02	0.15 ± 0.02	0.01 ± 0.05	0.06 ± 0.04	0.21 ± 0.03	–
HD 182694	−0.07 ± 0.04	−0.08 ± 0.02	0.03 ± 0.03	0.16 ± 0.02	0.16 ± 0.02	0.16 ± 0.04	–
HD 183124	−0.00 ± 0.05	0.01 ± 0.04	0.11 ± 0.02	0.17 ± 0.05	0.04 ± 0.06	0.14 ± 0.04	–
HD 185286	0.12 ± 0.04	0.25 ± 0.01	0.13 ± 0.03	0.18 ± 0.03	0.12 ± 0.05	0.52 ± 0.05	0.30 ± 0.05
HD 185351	0.01 ± 0.04	0.11 ± 0.02	0.15 ± 0.03	−0.06 ± 0.06	0.13 ± 0.03	0.29 ± 0.04	–
HD 187217	−0.03 ± 0.06	−0.10 ± 0.10	−0.03 ± 0.02	–	−0.07 ± 0.03	0.22 ± 0.04	–
HD 188537	0.05 ± 0.07	0.10 ± 0.03	0.12 ± 0.04	0.20 ± 0.04	0.15 ± 0.10	0.30 ± 0.04	–
HD 188629	0.10 ± 0.06	0.22 ± 0.01	0.10 ± 0.02	0.15 ± 0.03	0.06 ± 0.07	0.43 ± 0.01	0.34 ± 0.22
HD 188875	−0.02 ± 0.05	0.23 ± 0.02	0.09 ± 0.03	0.19 ± 0.07	0.20 ± 0.05	0.30 ± 0.03	–
HD 226754	0.19 ± 0.05	0.33 ± 0.03	0.23 ± 0.03	0.28 ± 0.07	−0.05 ± 0.07	0.34 ± 0.04	0.26 ± 0.13

(Montet & Simon 2016) and in relation to Harvard photographic plates from 1890 onwards (Schaefer 2016). The dimming, which is chromatic in the manner expected of heterogeneous clouds of circumstellar dust in the line of sight (Davenport et al. 2018; Bodman et al. 2018), has been ascribed to various causes (reviewed in Wright 2018), most notably a cloud of exocomets surrounding the star (e.g. Wyatt et al. 2018). It is unclear whether the explanation of the hump-and-spike phenomenon will shed light on the strange behaviour of Boyajian’s Star, but it may be relevant.

[Ashley/Dan/Vichi?](#)

3.2.3 Eclipsing Binaries

We detect some eclipsing binaries [Ben - finish this.](#)

4 OPEN SCIENCE

We believe in open science, and have therefore made all substantive products of this research available to the interested reader. All code used to produce smear light curves is available under a GPL v3 license at github.com/benjaminpope/keplersmear. All smear

light curves, both including the red giant sample studied in detail in Section 3.1, and main sequence stars as discussed in Sections 3.2.1 and 3.2.3, can be downloaded from the Mikulski Archive for Space Telescopes (MAST) as a High-Level Science Product. TRES spectra are available from [somewhere](#), and all asteroseismic parameters and derived stellar parameters for the red giants in Section 3.1 are provided in an online-only table as Supplementary Material to this paper.

All smear light curves in this paper, as well as the \LaTeX source code used to produce this document, can be found at github.com/benjaminpope/smearcampaign.

5 CONCLUSIONS

ACKNOWLEDGEMENTS

This work was performed in part under contract with the Jet Propulsion Laboratory (JPL) funded by NASA through the Sagan Fellowship Program executed by the NASA Exoplanet Science Institute. B.P. also acknowledges support from Balliol College and the Clarendon Fund. D.H. acknowledges support by the Australian Research Council’s Discovery Projects funding scheme (project num-

Table 6. Chemical abundances relative to iron for stars in the red giant sample as determined by BACCHUS, without differential line-by-line comparison to Arcturus, as described in Section 2.4, for the elements Zn, Y, Cr, V, Cu, and Sc. Dashes indicate elements for which abundances could not be reliably computed.

Object	[Zn/Fe]	[Y/Fe]	[Cr/Fe]	[V/Fe]	[Cu/Fe]	[Sc/Fe]
BD+36 3564	-0.29 ± 0.20	-0.27 ± 0.02	0.23 ± 0.00	0.15 ± 0.03	-0.04 ± 0.06	0.17 ± 0.02
BD+39 3577	-0.24 ± 0.71	-0.40 ± 0.04	0.16 ± 0.10	0.01 ± 0.02	-0.21 ± 0.01	-0.12 ± 0.05
BD+43 3064	–	-0.14 ± 0.05	0.32 ± 0.01	0.24 ± 0.03	-0.16 ± 0.10	0.14 ± 0.02
BD+43 3171	-0.40 ± 0.05	-0.31 ± 0.03	0.29 ± 0.04	0.12 ± 0.06	0.02 ± 0.11	0.14 ± 0.03
BD+43 3213	–	-0.06 ± 0.09	0.39 ± 0.01	0.08 ± 0.09	-0.28 ± 0.11	0.18 ± 0.04
BD+48 2955	–	-0.15 ± 0.05	0.23 ± 0.04	0.20 ± 0.03	-0.05 ± 0.04	0.15 ± 0.03
HD 174020	-0.48 ± 1.11	-0.19 ± 0.06	0.41 ± 0.06	0.26 ± 0.03	-0.20 ± 0.11	0.18 ± 0.03
HD 174829	-0.12 ± 0.13	-0.25 ± 0.06	0.16 ± 0.02	0.01 ± 0.02	-0.23 ± 0.03	0.12 ± 0.03
HD 175740	-0.16 ± 0.16	-0.09 ± 0.07	0.13 ± 0.04	0.09 ± 0.02	-0.16 ± 0.04	0.08 ± 0.03
HD 175884	-0.15 ± 0.17	-0.21 ± 0.07	0.26 ± 0.04	0.21 ± 0.02	-0.10 ± 0.05	0.13 ± 0.02
HD 178797	–	-0.08 ± 0.05	0.26 ± 0.04	0.19 ± 0.02	-0.11 ± 0.04	0.23 ± 0.03
HD 178910	-0.29 ± 0.74	-0.18 ± 0.05	0.29 ± 0.01	0.17 ± 0.02	0.21 ± 0.14	0.14 ± 0.02
HD 179396	-0.07 ± 0.15	-0.27 ± 0.07	0.12 ± 0.03	0.03 ± 0.02	-0.16 ± 0.06	0.10 ± 0.03
HD 179959	0.05 ± 1.84	-0.08 ± 0.06	-0.00 ± 0.03	-0.11 ± 0.02	-0.29 ± 0.05	0.10 ± 0.05
HD 180312	-0.18 ± 0.01	-0.23 ± 0.05	-0.06 ± 0.06	-0.05 ± 0.02	-0.15 ± 0.04	0.15 ± 0.05
HD 180475	-0.09 ± 0.11	-0.25 ± 0.08	0.24 ± 0.04	0.20 ± 0.02	-0.00 ± 0.04	0.21 ± 0.03
HD 180658	0.16 ± 1.25	-0.20 ± 0.01	0.19 ± 0.04	0.15 ± 0.02	-0.05 ± 0.06	0.12 ± 0.03
HD 180682	-0.23 ± 0.14	-0.29 ± 0.04	0.23 ± 0.03	0.26 ± 0.02	-0.06 ± 0.04	0.27 ± 0.02
HD 181022	-0.27 ± 0.03	-0.23 ± 0.02	0.19 ± 0.08	0.10 ± 0.08	-0.01 ± 0.12	0.25 ± 0.04
HD 181069	-0.02 ± 0.19	-0.11 ± 0.08	0.22 ± 0.03	0.15 ± 0.02	-0.10 ± 0.05	0.13 ± 0.03
HD 181097	-0.08 ± 0.41	-0.21 ± 0.03	0.25 ± 0.02	0.19 ± 0.03	-0.12 ± 0.03	0.22 ± 0.03
HD 181597	-0.14 ± 0.15	-0.19 ± 0.08	0.19 ± 0.05	0.21 ± 0.02	-0.18 ± 0.04	0.16 ± 0.02
HD 181778	-0.03 ± 0.18	-0.13 ± 0.04	0.18 ± 0.02	-0.02 ± 0.02	-0.25 ± 0.07	0.05 ± 0.02
HD 181880	-0.04 ± 0.22	-0.20 ± 0.07	0.27 ± 0.03	0.22 ± 0.02	-0.07 ± 0.03	0.23 ± 0.03
HD 182531	0.03 ± 0.78	-0.19 ± 0.07	0.29 ± 0.05	0.24 ± 0.03	-0.08 ± 0.05	0.18 ± 0.02
HD 182692	-0.24 ± 1.34	-0.21 ± 0.10	0.15 ± 0.07	0.24 ± 0.02	-0.11 ± 0.06	0.18 ± 0.03
HD 182694	-0.24 ± 0.07	-0.12 ± 0.05	0.04 ± 0.03	-0.05 ± 0.02	-0.26 ± 0.04	0.09 ± 0.05
HD 183124	-0.18 ± 0.17	-0.24 ± 0.03	0.12 ± 0.04	0.10 ± 0.02	-0.22 ± 0.02	0.10 ± 0.03
HD 185286	–	-0.19 ± 0.08	0.46 ± 0.01	0.34 ± 0.02	-0.11 ± 0.10	0.27 ± 0.03
HD 185351	-0.31 ± 0.10	-0.16 ± 0.05	0.16 ± 0.04	0.18 ± 0.02	-0.17 ± 0.03	0.12 ± 0.04
HD 187217	–	-0.37 ± 0.05	0.28 ± 0.03	0.11 ± 0.03	-0.23 ± 0.02	0.04 ± 0.05
HD 188537	0.32 ± 0.78	-0.27 ± 0.09	0.17 ± 0.01	0.11 ± 0.02	-0.17 ± 0.04	0.06 ± 0.05
HD 188629	–	-0.04 ± 0.10	0.30 ± 0.06	0.31 ± 0.04	-0.15 ± 0.09	0.22 ± 0.04
HD 188875	0.31 ± 1.71	-0.04 ± 0.07	0.33 ± 0.07	0.18 ± 0.02	-0.25 ± 0.07	0.13 ± 0.03
HD 226754	-0.22 ± 1.07	-0.33 ± 0.04	0.38 ± 0.07	0.45 ± 0.04	-0.02 ± 0.07	0.30 ± 0.04

ber DE140101364) and support by the NASA Grant NNX14AB92G issued through the *Kepler* Participating Scientist Program.

BP acknowledges being on the traditional territory of the Lenape Nations and, today, we recognize that Manhattan continues to be the home to many Algonkian peoples. We thank the Lenape peoples for allowing us to carry out this work on the Lenape original homelands at New York University. BP and TW would like to acknowledge the Gadigal people of the Eora Nation and the Norongerragal and Gweagal peoples of the Tharawal Nation as the traditional owners of the land at the University of Sydney and the Sutherland Shire on which some of this work was carried out, and pay their respects to their knowledge, and their elders past, present and future.

This work has made use of data from the European Space Agency (ESA) mission *Gaia* (<https://www.cosmos.esa.int/gaia>), processed by the *Gaia* Data Processing and Analysis Consortium (DPAC, <https://www.cosmos.esa.int/web/gaia/dpac/consortium>). Funding for the DPAC has been provided by national institutions, in particular the institutions participating in the *Gaia* Multilateral Agreement. This work has in particular made use of the [gaia-kepler.fun](https://github.com/gaia-kepler.fun) crossmatch database created by Megan Bedell.

This research made use of NASA’s Astrophysics Data Sys-

tem; the SIMBAD database, operated at CDS, Strasbourg, France; the IPython package (Pérez & Granger 2007); SciPy (Jones et al. 2001); and Astropy, a community-developed core Python package for Astronomy (Astropy Collaboration et al. 2013). Some of the data presented in this paper were obtained from the Mikulski Archive for Space Telescopes (MAST). STScI is operated by the Association of Universities for Research in Astronomy, Inc., under NASA contract NAS5-26555. Support for MAST for non-HST data is provided by the NASA Office of Space Science via grant NNX13AC07G and by other grants and contracts. We acknowledge the support of the Group of Eight universities and the German Academic Exchange Service through the Go8 Australia-Germany Joint Research Co-operation Scheme.

REFERENCES

- Aerts C., et al., 2018, *MNRAS*, **476**, 1234
Aigrain S., Parviainen H., Pope B. J. S., 2016, *MNRAS*, **459**, 2408
Alvarez R., Plez B., 1998, *A&A*, **330**, 1109
Ambikasaran S., Foreman-Mackey D., Greengard L., Hogg D. W., O’Neil M., 2015, *IEEE Transactions on Pattern Analysis and Machine Intelligence*, **38**

- Angus R., Aigrain S., Foreman-Mackey D., McQuillan A., 2015, *MNRAS*, **450**, 1787
- Astropy Collaboration et al., 2013, *A&A*, **558**, A33
- Bailer-Jones C. A. L., Rybizki J., Fournesneau M., Mantelet G., Andrae R., 2018, preprint, ([arXiv:1804.10121](https://arxiv.org/abs/1804.10121))
- Beck P. G., et al., 2011, *Science*, **332**, 205
- Beck P. G., et al., 2012, *Nature*, **481**, 55
- Bedding T. R., et al., 2011, *Nature*, **471**, 608
- Blanco-Cuaresma S., Soubiran C., Jofré P., Heiter U., 2014, *A&A*, **566**, A98
- Bodman E., Wright J., Boyajian T., Ellis T., 2018, preprint, ([arXiv:1806.08842](https://arxiv.org/abs/1806.08842))
- Borucki W. J., et al., 2010, *Science*, **327**, 977
- Boyajian T. S., et al., 2016, *MNRAS*, **457**, 3988
- Brown T. M., Latham D. W., Everett M. E., Esquerdo G. A., 2011, *AJ*, **142**, 112
- Buchhave L. A., et al., 2012, *Nature*, **486**, 375
- Campante T. L., et al., 2015, *ApJ*, **799**, 170
- Casagrande L., et al., 2014, *MNRAS*, **439**, 2060
- Chaplin W. J., Miglio A., 2013, *ARA&A*, **51**, 353
- Christiansen J. L., et al., 2012, *PASP*, **124**, 1279
- Creevey O. L., et al., 2013, *MNRAS*, **431**, 2419
- Creevey O. L., et al., 2015, *A&A*, **575**, A26
- Davenport J. R. A., et al., 2018, *ApJ*, **853**, L30
- Davies G. R., Miglio A., 2016, *Astronomische Nachrichten*, **337**, 774
- Davies G. R., et al., 2017, *A&A*, **598**, L4
- Farr W. M., et al., 2018, preprint, ([arXiv:1802.09812](https://arxiv.org/abs/1802.09812))
- Foreman-Mackey D., Hogg D. W., Morton T. D., 2014, *ApJ*, **795**, 64
- Fressin F., et al., 2013, *ApJ*, **766**, 81
- Gaia Collaboration et al., 2016, *A&A*, **595**, A1
- Gaia Collaboration Brown A. G. A., Vallenari A., Prusti T., de Bruijne J. H. J., Babusiaux C., Bailer-Jones C. A. L., 2018, preprint, ([arXiv:1804.09365](https://arxiv.org/abs/1804.09365))
- García R. A., et al., 2011, *MNRAS*, **414**, L6
- Gilliland R. L., et al., 2010, *PASP*, **122**, 131
- Girardi L., 2016, *ARA&A*, **54**, 95
- Gustafsson B., Edvardsson B., Eriksson K., Jørgensen U. G., Nordlund Å., Plez B., 2008, *A&A*, **486**, 951
- Harvey J., 1985, in Rolfe E., Battick B., eds, *ESA Special Publication Vol. 235, Future Missions in Solar, Heliospheric & Space Plasma Physics*.
- Hawkins K., et al., 2016a, *A&A*, **592**, A70
- Hawkins K., et al., 2016b, *A&A*, **592**, A70
- Hawkins K., Masseron T., Jofré P., Gilmore G., Elsworth Y., Hekker S., 2016c, *A&A*, **594**, A43
- Hawkins K., Leistedt B., Bovy J., Hogg D. W., 2017, *MNRAS*, **471**, 722
- Heiter U., Jofré P., Gustafsson B., Korn A. J., Soubiran C., Thévenin F., 2015, *A&A*, **582**, A49
- Hinkel N. R., Timmes F. X., Young P. A., Pagano M. D., Turnbull M. C., 2014, *AJ*, **148**, 54
- Hjørringgaard J. G., Silva Aguirre V., White T. R., Huber D., Pope B. J. S., Casagrande L., Justesen A. B., Christensen-Dalsgaard J., 2017, *MNRAS*, **464**, 3713
- Howell S. B., et al., 2014, *PASP*, **126**, 398
- Huber D., et al., 2012, *ApJ*, **760**, 32
- Huber D., et al., 2013, *ApJ*, **767**, 127
- Jofré P., 2016, *Astronomische Nachrichten*, **337**, 859
- Jofré P., et al., 2014, *A&A*, **564**, A133
- Jofré P., et al., 2015, *A&A*, **582**, A81
- Jofré P., et al., 2017, *A&A*, **601**, A38
- Jones E., Oliphant T., Peterson P., Others 2001, *SciPy: Open source scientific tools for Python*, <http://www.scipy.org/>
- Kallinger T., et al., 2014, *A&A*, **570**, A41
- Kjeldsen H., Bedding T. R., 1995, *A&A*, **293**, 87
- Koch D. G., et al., 2010, *ApJ*, **713**, L79
- Kolodziejczak J., Caldwell D., 2011, Technical Report 20120003045, Science from Kepler Collateral Data: 150 ksec/year from 13 Million Stars?, <http://ntrs.nasa.gov/archive/nasa/casi.ntrs.nasa.gov/20120003045.pdf>. NASA Marshall Space Flight Center, <http://ntrs.nasa.gov/archive/nasa/casi.ntrs.nasa.gov/20120003045.pdf>
- Lindegren L., et al., 2018, preprint, ([arXiv:1804.09366](https://arxiv.org/abs/1804.09366))
- Lomb N. R., 1976, *Ap&SS*, **39**, 447
- Lund M. N., et al., 2016, preprint, ([arXiv:1612.00436](https://arxiv.org/abs/1612.00436))
- Masseron T., et al., 2014, *A&A*, **571**, A47
- Masseron T., Merle T., Hawkins K., 2016, BACCHUS: Brussels Automatic Code for Characterizing High accuracy Spectra, Astrophysics Source Code Library (ascl:1605.004), doi:10.20356/C4TG6R
- Montet B. T., Simon J. D., 2016, *ApJ*, **830**, L39
- Pérez F., Granger B. E., 2007, *Computing in Science and Engineering*, **9**, 21
- Petigura E. A., Marcy G. W., 2012, *PASP*, **124**, 1073
- Petigura E. A., Howard A. W., Marcy G. W., 2013, *Proceedings of the National Academy of Science*, **110**, 19273
- Plez B., 2012, Turbospectrum: Code for spectral synthesis, Astrophysics Source Code Library (ascl:1205.004)
- Pope B. J. S., et al., 2016, *MNRAS*, **455**, L36
- Ruiz-Dern L., Babusiaux C., Arenou F., Turon C., Lallement R., 2018, *A&A*, **609**, A116
- Saio H., Kurtz D. W., Murphy S. J., Antoci V. L., Lee U., 2018, *MNRAS*, **474**, 2774
- Scargle J. D., 1982, *ApJ*, **263**, 835
- Schaefer B. E., 2016, *ApJ*, **822**, L34
- Silva Aguirre V., et al., 2013, *ApJ*, **769**, 141
- Silva Aguirre V., et al., 2015, *MNRAS*, **452**, 2127
- Silva Aguirre V., et al., 2016, preprint, ([arXiv:1611.08776](https://arxiv.org/abs/1611.08776))
- Smith J. C., et al., 2012, *PASP*, **124**, 1000
- Stumpe M. C., et al., 2012, *PASP*, **124**, 985
- Twicken J. D., Chandrasekaran H., Jenkins J. M., Gunter J. P., Girouard F., Klaus T. C., 2010, in *Software and Cyberinfrastructure for Astronomy*, p. 77401U, doi:10.1117/12.856798
- Van Eylen V., Agentoft C., Lundkvist M. S., Kjeldsen H., Owen J. E., Fulton B. J., Petigura E., Snellen I., 2018, *MNRAS*, **479**, 4786
- White T. R., et al., 2013, *MNRAS*, **433**, 1262
- White T. R., et al., 2015, in *European Physical Journal Web of Conferences*, p. 06068, doi:10.1051/epjconf/201510106068
- White T. R., et al., 2017, *MNRAS*, **471**, 2882
- Wright J. T., 2018, *Research Notes of the American Astronomical Society*, **2**, 16
- Wyatt M. C., van Lieshout R., Kennedy G. M., Boyajian T. S., 2018, *MNRAS*, **473**, 5286
- van Leeuwen F., 2007, *A&A*, **474**, 653
- van Saders J. L., Ceillier T., Metcalfe T. S., Silva Aguirre V., Pinsonneault M. H., García R. A., Mathur S., Davies G. R., 2016, *Nature*, **529**, 181

This paper has been typeset from a \LaTeX file prepared by the author.